SANDIA REPORT

SAND2011-7315
Unlimited Release
Printed October 2011

Room Temperature Detector Array Technology for the Terahertz to Far-infrared

Eric A. Shaner, Emil Kadlec, Jeremy Wright, Hu Tao, Richard Averitt, X. Zhang, Doug Trotter, Mike Shaw, Tony Lentine, Peter Rakich, and Ryan Camacho

Prepared by
Sandia National Laboratories
Albuquerque, New Mexico 87185 and Livermore, California 94550

Sandia National Laboratories is a multi-program laboratory managed and operated by Sandia Corporation, a wholly owned subsidiary of Lockheed Martin Corporation, for the U.S. Department of Energy's National Nuclear Security Administration under contract DE-AC04-94AL85000.

Issued by Sandia National Laboratories, operated for the United States Department of Energy by Sandia Corporation.

Available to DOE and DOE contractors from
U.S. Department of Energy
Office of Scientific and Technical Information
P.O. Box 62
Oak Ridge, TN 37831

Telephone: (865) 576-8401
Facsimile: (865) 576-5728
E-Mail: reports@adonis.osti.gov
Online ordering: http://www.osti.gov/bridge

Available to the public from
U.S. Department of Commerce
National Technical Information Service
5285 Port Royal Rd.
Springfield, VA 22161

Telephone: (800) 553-6847
Facsimile: (703) 605-6900
E-Mail: orders@ntis.fedworld.gov
Online order: http://www.ntis.gov/help/ordermethods.asp?loc=7-4-0#online

SAND2011-7315
Unlimited Release
Printed October 2011

Room Temperature Detector Array Technology for the Terahertz to Far-infrared

Eric A. Shaner, Emil Kadlec, Jeremy Wright, Hu Tao, Richard Averitt, X. Zhang, Doug Trotter, Mike Shaw, Tony Lentine, Peter Rakich, and Ryan Camacho

Sandia National Laboratories
P.O. Box 5800
Albuquerque, New Mexico 87185-MS1415

Abstract

Thermal detection has made extensive progress in the last 40 years, however, the speed and detectivity can still be improved. The advancement of silicon photonic microring resonators has made them intriguing for detection devices due to their small size and high quality factors. Implementing silicon photonic microring or microdisk resonators as a means of a thermal detector gives rise to higher speed and detectivity, as well as lower noise compared to conventional devices with electrical readouts. This LDRD effort explored the design and measurements of silicon photonic microdisk resonators used for thermal detection. The characteristic values, consisting of the thermal time constant ($\tau \approx 2$ ms) and noise equivalent power were measured and found to surpass the performance of the best microbolometers. Furthermore the detectivity was found to be $D_\lambda = 2.47 \times 10^8$ cm·√Hz/W at 10.6 μm which is comparable to commercial detectors. Subsequent design modifications should increase the detectivity by another order of magnitude. Thermal detection in the terahertz (THz) remains underdeveloped, opening a door for new innovative technologies such as metamaterial enhanced detectors. This project also explored the use of metamaterials in conjunction with a cantilever design for detection in the THz region and demonstrated the use of metamaterials as custom thin film absorbers for thermal detection. While much work remains to integrate these technologies into a unified platform, the early stages of research show promising futures for use in thermal detection.

CONTENTS

NOMENCLATURE

FIRL	Far infrared laser
FTIR	Fourier Transform Infrared Spectrometer
MM	Metamaterial
PSD	position sensitive detector
Q	Resonator quality factor
SRR	split ring resonator
TMFPA	Thermal Microphotonic Focal Plane Array
THz-TDS	Terahertz time domain spectroscopy
VDI	Virginia Diodes

1. BACKGROUND

1.1. Motivation

The terahertz (THz) to far-infrared portion of the electromagnetic spectrum extends from roughly 100 GHz to 30 THz (where 1 THz corresponds to a wavelength of 300 microns and photon energy of 4.1 meV). From radio frequency waves through X-rays, this portion of the electromagnetic spectrum is the least developed and therefore the least understood scientifically and technologically. Detection of THz radiation at elevated temperatures is a complicated due to the low excitation energies involved (ruling out more standard semiconductor based detection schemes). Our goal in this effort was to develop a path towards room temperature detector solutions that are amenable to integration in a focal plane array. This included verification of a Sandia developed technology, the thermal microphotonic focal plane array (TMFPA, SAND2009-6998) and the exploration of thin film metamaterial enhanced absorber elements that can be integrated into the TMFPA or other similar microbolometer platforms.

2. ACCOMPLISHMENTS

2.1: Thermal Microphotonic Focal Plane Array (TMFPA) Pixel Verification

Platform

The high quality factors (Q) of optical microring resonators have enabled the design and demonstration of highly sensitive microring-resonator-based sensors. Examples include chemical, biological, nuclear, inertial, and thermal sensors [1-5]. In the case of the thermal detector, a temperature change in the resonator will induce a change in the index of refraction (n) of the disk causing a corresponding change in the resonance wavelength of the microdisk. The change in resonance will ultimately cause a change in transmission of the bus waveguide which is measured with a basic optical power detector. The microdisk resonator thermal detector is shown in Fig. 2.1.1.

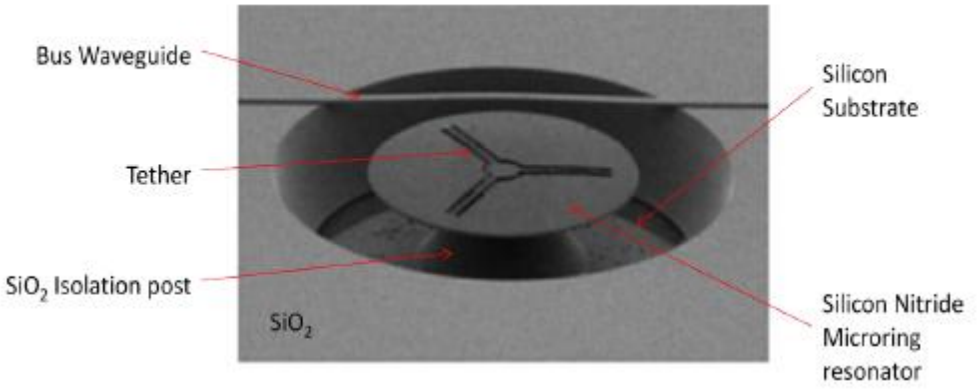

Fig 2.1.1: TMFPA pixel showing microdisk and bus waveguide

Figure 2.1.1 displays the important components of the IR microring resonator thermal detector. These components include the absorber, bus waveguide, and insulating post. The insulating post isolates the microring from the substrate thereby reducing the thermal flux (noise) from the microring to the substrate. The thermal noise, also known as phonon noise, is expressed by Eq. 1 as Noise Equivalent Power (NEP). Physically this noise arises from the passage of quantized carriers of energy through the thermal linkage; this movement causes white noise (frequency independent noise)[6].

$$NEP_{phonon} = \sqrt{4k_B G}T \qquad (1)$$

In the case of the microdisk resonator thermal detector G is the thermal conductance of the insulating post and support structure which is specific to design, k_B is the Boltzmann constant, and T is temperature expressed in Kelvin. The noise floor of the detector does not include any Johnson noise due to the absence of electronic evaluation. The elimination of the Johnson noise improves the overall noise performance of this device giving it a potential edge over current commercially available thermal detectors. The thermal conductance of the tethers is on the order of $10^{-7}W/K$.

Planar Disk Resonators

The waveguide serves as a medium for the interrogation light to pass through for inspection of the microdisk. The interrogation light evanescently couples to the microdisk

from the waveguide. The resonant wavelength of the ring resonator is given in Eq. 2**Error! Reference source not found.**, where n_{eff} is the effective refractive index of the disk mode, r is the radius of the disk, and N is an integer.

$$\lambda_{res} = \frac{2 \cdot \pi \cdot r \cdot n_{eff}}{N} \qquad (2)$$

The fixed wavelength interrogation light in the bus waveguide is intended to measure a shift in resonance which is directly related to a change in the resonance of the ring. The change in the resonance of the ring is caused by a change in the effective refractive index upon heating due to absorption of radiation is described by Eq. 3 where FSR is the free spectral range of the ring and λ_o is the resonance wavelength [5].

$$\Delta\lambda = \frac{\Delta n_{eff} \cdot FSR \cdot \pi \cdot r}{\lambda_o} \qquad (3)$$

The change in resonance due to heating of the disk will change the transmission of the interrogation light. Ultimately the change in transmission will lead to a change in power received by a photodetector which is then interpreted as a photoresponse.

Quality Factor

The responsivity resolution of these devices is characterized by the quality factor (Q). The quality factor is expressed in **Error! Reference source not found.** 4 where λ_O is the resonance wavelength and λ_{FWHM} is the full width at half maximum of the resonance.

$$\boldsymbol{Q} \approx \frac{\lambda_O}{\lambda_{FWHM}} \quad (4)$$

As Q is increased the signal increases equally as well as the noise due to resonance fluctuations. It is important to note this characteristic of Q for future designs as changing the Q only changes the responsivity of the device and not the NEP. However, in multipixel arrangements and when considering overall system noise, higher Q values will result in improved performance.

Measurement Setup

A custom designed vacuum chamber was used for the testing of the microdisk resonator thermal detector. As seen in **Error! Reference source not found.** 2.1.2, the vacuum apparatus consists of ports for optical fibers, electronics, vacuum, and a window for thermal interrogation. The inside of the chamber contains an optical bread board for mounting. Also inside of the chamber are two electrically driver 3-axis stages, a thermoelectric cooler, and a one-axis stage for sample mounting. During measurements the chamber is evacuated to pressures in the 10^{-5} Torr range. This evacuation improves the thermal resistance of the resonator disc from the substrate. The optical feed-throughs are for the input of the interrogation laser (nominally 1550 nm). The feed-throughs are connected to lensed fibers which are for coupling the interrogation laser into the bus waveguide. The lensed fibers are aligned using the 3-axis stages. The electrical feed-through is for the electric wiring of the multiple stage motors and the thermoelectric cooler. The window of the apparatus is designed for high transmission of long-wave infrared radiation. The measured transmission of the window was $T_{window} = 0.7$. The source of the radiation was a temperature controlled CO_2 laser operating at 10.6μm. The CO_2 laser was internally chopped, referenced by a TTL signal to produce a square-wave output. Before interrogation of the microring resonator the laser power must be

attenuated. This was done by the use of a 0.99 reflection optic and a wire-grid polarizer pair. The polarizer pair is in place for simple user controllable power. The beam is then brought into the vacuum chamber perpendicularly by an optical mirror mounted to a microscope head. The beam is purposely not focused to promote flood illumination of the resonator. The CO_2 radiation is absorbed by the SiN_x resonator disk which leads to heating and therefore a shift of resonance. To measure the sensitivity of the resonator we must know the incident CO_2 power on the disk. To do so a beam image and power measurements were acquired. The image was taken using the commercially bought Pyrocam; **Error! Reference source not found.** shows an image of the CO_2 beam.

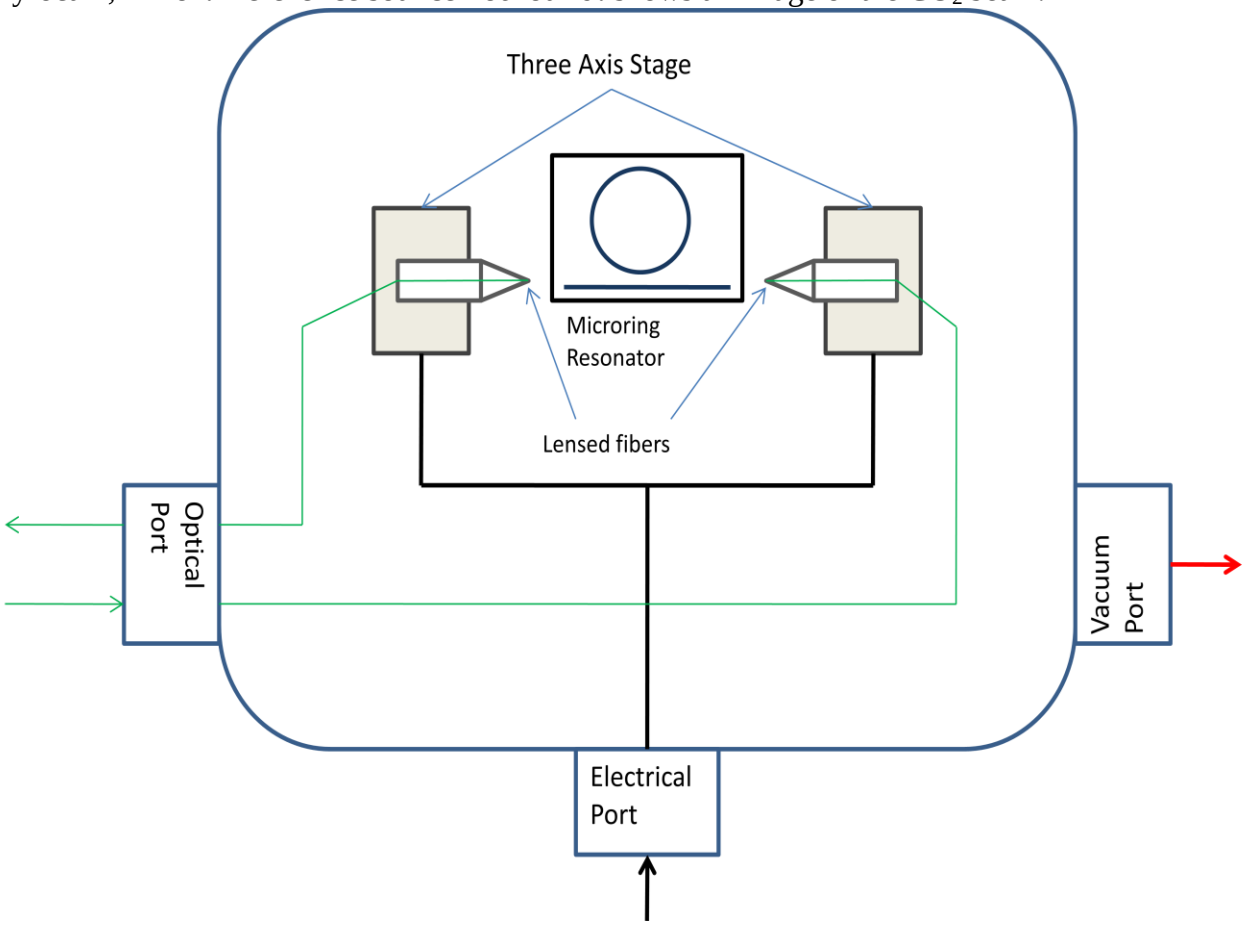

Fig. 2.1.2 Schematic of the vacuum assembly showing optical, electrical and vacuum ports

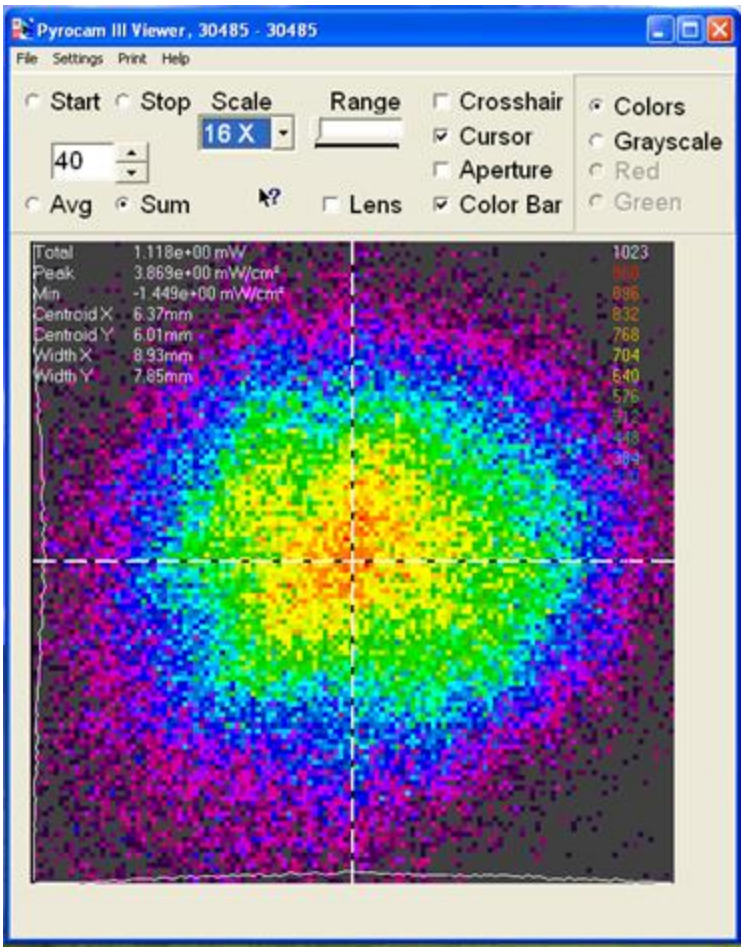

Fig. 2.1.3 Image of CO_2 beam taken with the Pyrocam

The measured beam diameter was 8.93 mm with a full width half maximum (FWHM) of 6.25 mm. The beam profile is also seen to be Gaussian. The measured incident power onto the window was 3.71 mW. Using a Gaussian approximation the incident power on the disk was calculated. **Error! Reference source not found.** is the Gaussian profile used for the calculation

$$\boldsymbol{I}(\rho) = A\exp(-\frac{\rho^2}{2c^2}). \quad (5)$$

$$\boldsymbol{c} = FWHM/\sqrt{8\ln 2} \quad (6)$$

Equation 5 is expressed in cylindrical coordinates to simplify the integration to solve for incident power per unit area A. Solving Eq. 6 we find $c = 2.7\,mm$. To solve for the coefficient A integration of the Gaussian function over the range of $\rho[0,\infty)$ and $\theta[0,2\pi]$ was made.

$$P_{total} = \iint_{0\,0}^{2\pi\,\infty} A\exp(-\frac{\rho^2}{2c^2})\rho d\rho d\theta = \mathbf{2}\pi A 2c^2(1-0) = 4\pi c^2 A \quad (7)$$

Solving for **Error! Reference source not found.** 7 we find A = 45.29mW/m^2. Finally we can again perform integration on Eq. 5 to solve for the incident power on the disk by integrating over the range $\rho[0,10\mu m], \theta[0,2\pi]$. The solution of the integral is the incident power of a $20\,\mu m$ diameter circle centered in the Gaussian beam on the window of the chamber, $P' = 0.2676\,nW$. Finally to solve for the incident power on the disc P' is

multiplied by the transmission of the window, $P_D = P'T_{window}$. The incident power on the disc was found to be $P_D = 0.1845\ nW$.

Measurements

The interrogation laser wavelength must rest on the 3dB point of a side of the resonance of the microdisk resonator for optimum response.

shows the resonance of the microdisk. This may be achieved in two different ways: (1) by thermally changing the resonance of the disc by means of the thermoelectric cooler or (2) by changing the wavelength of the laser. Either way the thermoelectric cooler must be used to ensure large temperature fluctuations do not occur as this would add environmental noise. The method chosen was to thermoelectrically stabilize the temperature while supplying an adjustable wavelength interrogation laser. The transmitted power through the bus waveguide was measured with the New Focus 2053 photoreceiver. The output of the photoreceiver was evaluated using either the SR785 Lock-in-amplifier or the SR850 spectrum analyzer. Generally the Lock-in-amplifier was used during the CO_2 alignment because of the ability for low integration times and to lock-in on the chopping frequency. The spectrum analyzer was used to measure the spectrum of the system for noise analysis. Fig. 2.1.5 shows a spectrum of the resonator given by the SR785 spectrum analyzer. The noise below 60Hz is thought to be due to mechanical vibrations in the system.

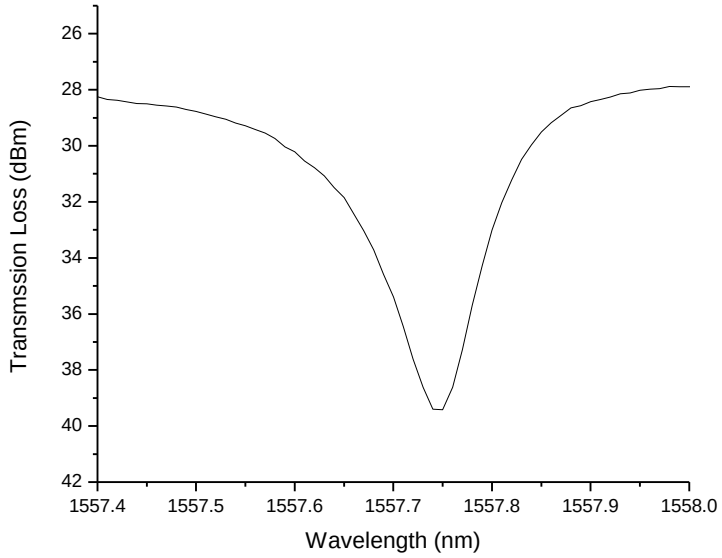

Fig 2.1.4: Resonance of microdisk resonator

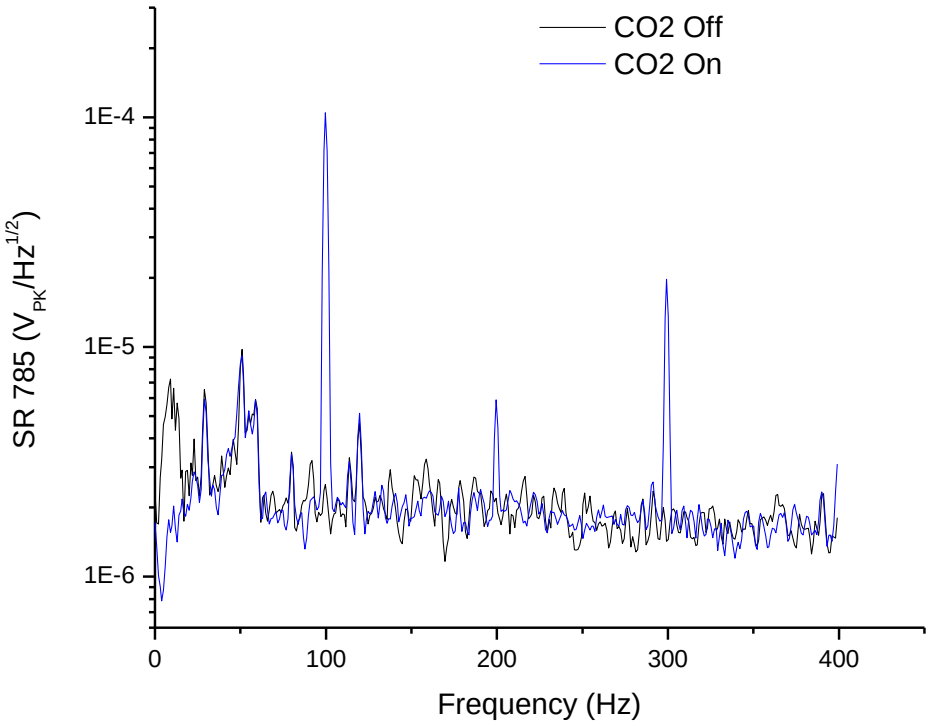

Fig 2.1.5: Spectral Plot of Resonator (Output of SR785)

The important characterizations of thermal detectors are time constant (τ), responsivity ($\mathcal{R}$), noise equivalent power (NEP), and specific spectral detectivity ($\mathcal{D}_\lambda$). The time constant was found to be 2ms. This time constant is a fraction of the best commercially available thermal detectors which range from 10 – 40ms[8]. The signal voltage of the detector was measured using the SR785 spectrum analyzer and was found to be $V_{Signal} = 109.477\mu V$. The SR785 references the input signal to a sine-wave; therefore the square-wave input into the SR785 is broken into separate sinusoidal harmonics. **Error! Reference source not found.** shows the Fourier series of the square-wave where n is the harmonic of the square-wave.

$$\boldsymbol{a}(t) = \frac{4}{\pi}\sum_{n=1}^{\infty}\frac{1}{n}\sin 2n\pi ft \quad (8)$$

The power of the first harmonic is given by **Error! Reference source not found.** where the transfer function of the square-wave is $F(\omega_1) = \frac{1}{1+j\omega\tau}$.

$$P_1 = \frac{P_{Disc}|F(\omega_1)|}{\sum_{n=1}^{\infty}\frac{1}{n}|F(\omega_n)|} \quad (9)$$

For a chopping frequency of 100Hz the power of the first harmonic is calculated to be $P_1 = 97.84\,pW$. The responsivity is calculated to be $\mathcal{R} = 1.12 \times 10^6 V/W$.

NEP and Detectivity Calculation

Noise equivalent power (NEP) is a calculation to determine the minimal amount of signal detectable, in other words where the signal-to-noise ratio is unity. The noise of the detector system was calculated using the SR850 to measure the spectral power density. The noise was measured with the CO_2 beam blocked. The measured noise was $N = 8\mu V/\sqrt{Hz}$ at 100Hz. As a result the NEP of the system was calculated to be $NEP = 7.15 \times 10^{-12}\, W/\sqrt{Hz}$. This NEP is a good start for a system which has much room to grow and provides a means of comparison of different detector types. The area of the detector is $3.14159 \times 10^{-6}\,\text{cm}^2$. The calculated specific detectivity is $\mathcal{D}_\lambda = 2.47 \times 10^8 \frac{cm\sqrt{Hz}}{W}$; this detectivity is on the order of the best commercial thermal detectors ($\mathcal{D}_\lambda^{comm} = 4 \times 10^8 \frac{cm\sqrt{Hz}}{W}$). The average bolometer pixel size is $12.25 \times 10^{-6} cm^2$ almost four times larger than the microdisk resonator, although the trend is moving towards smaller pixel sizes.

Design Improvements

The TMFPA pixels measured in this work were from the first installment of microdisk resonators for thermal detection[7]; therefore there are many improvements that could be made to the design. Current commercial detectors have high reflectance material underneath the thermal sensor to improve absorption in the detector element. For better detection a high reflectance material could be placed in the design of the microdisk resonator. Currently the spacing between the disc and substrate is about $10\mu m$ which was found through simulation has an absorption of only about 7.5%. **Error! Reference source not found.**2.1.6 shows simulation results for absorption at different substrate to resonator spacings. For LWIR detection it would be best to have a spacing of 7.5µm. The relatively low quality factor, Q = 15000, could be increased to obtain a higher responsivity, although the quality factor will not change internal NEP a smaller FWHM of the resonance would allow for a greater number of resonators to be placed on a single bus waveguide. A more experimental investigation should be made to find the relation of Q to the size of the tethers of the microdisk. To increase the time response the overall size of the microdisk could be made smaller by using a higher index material as the medium.

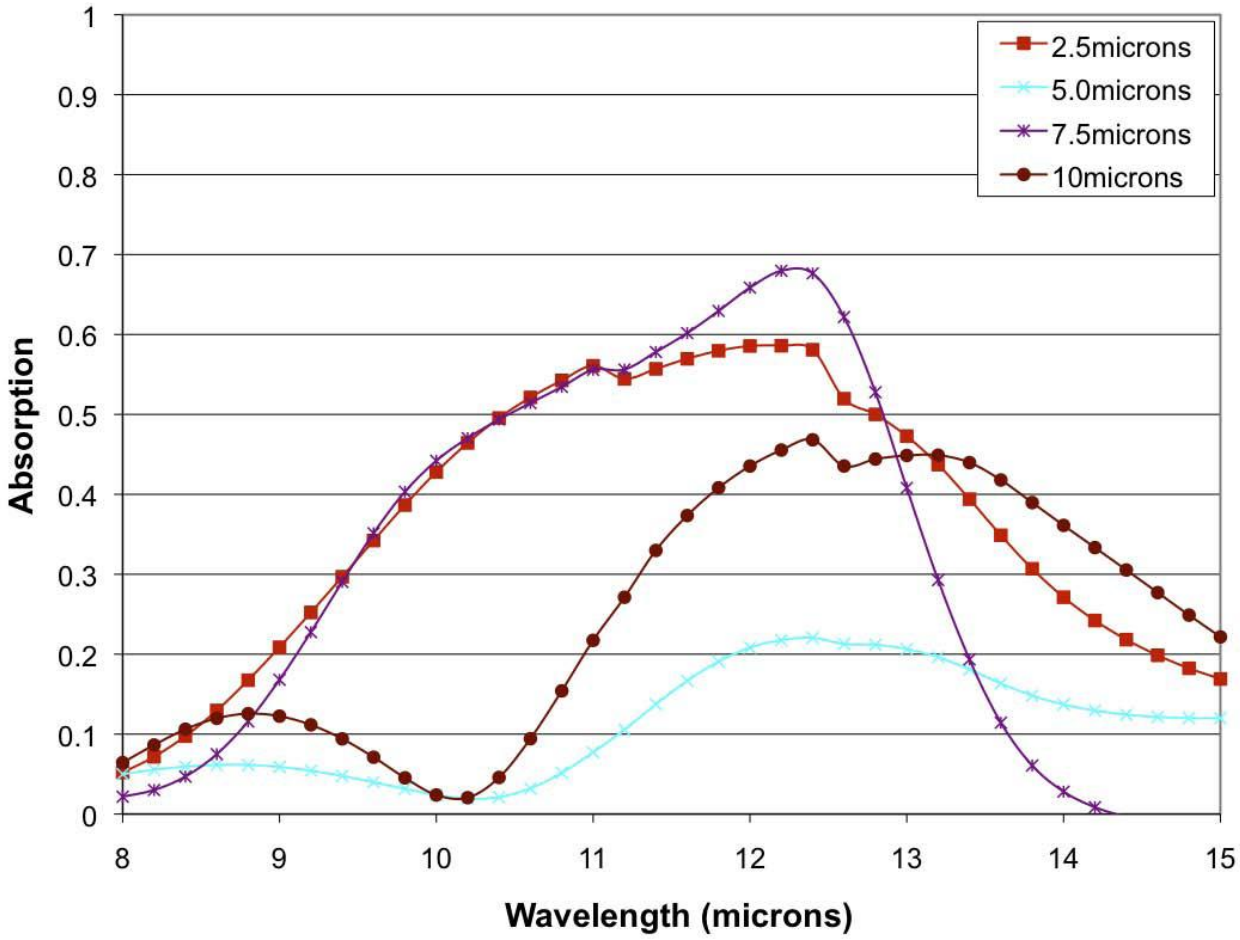

Fig. 2.1.6: Absorption as modeled by a 3D Rigorous Coupled Wave Analysis (RCWA) for a 200nm thick 20um diameter, silicon nitride resonator above a silicon substrate. The separate plots are for different substrate to detector spacing. [6]

2.2: Metamaterial Enhanced Thermal Detectors

Metamaterials

Recently, engineered materials composed of designed inclusions exhibiting unique electromagnetic (EM) properties not readily occurring in nature have attracted extraordinary interest from a wide group of scientists working in optics, physics, engineering, and material science[9]. Since the first demonstration of negative refractive index using metamaterials (MMs), world-wide effort has spawned numerous research thrusts resulting in advances such as super lenses and invisibility cloaks[10-14]. Sub-wavelength metamaterial elements can be tailored to provide a specific EM response at virtually any desired frequency[15]. As effective media, MMs can be characterized by a complex refractive index $n = n_1 + in_2$ where n_1 is related to the phase velocity and n_2 to losses[16]. A large fraction of MM research has focused on applications related to engineering n_1 (e.g. negative refractive index) while at the same time minimizing n_2 and the associated losses. However, manipulating the loss through judicious design of effective n_2 is advantageous for certain applications as demonstrated with recent work on perfect absorbers[17-19]. For example, designing a compact absorbing element can lead to enhanced functionality of EM detectors. The work that follows in this section was done in collaboration with Boston University.

Detector Design

Two different detection systems were fabricated and tested, the first designed for a resonant frequency of 95GHz (microwave spectrum) and the second at 693GHz (THz spectrum). The SRR for 95GHz detection was designed as a basic square SRR. The dimensions of the SRR can be seen in Fig. 2.2.1. A 50μm x 50μm optical pad was added to the SRR layout for the ability to optically interrogate the SRR system. The optical pad is meant to reflect an interrogation laser for measurement purposes. The SRR is fabricated onto a cantilever. The cantilever is designed with two bimorph arms supporting the SRR. At resonant frequencies small currents are induced in the SRR which will produce heat, due to the bimorph arms of the cantilever the heat will cause stress in the arms and therefore change the angle of the optical pad. The bimorph arms are fabricated using a deposition of gold on top of a silicon nitride layer. The combination of the cantilever and SRR are considered a unit cell or pixel. The spacing of a unit cell was 500μm. The 693GHz SRR was designed in much the same way as the 95GHz SRR except the overall size is smaller due to the shorter wavelength of resonance. The capacitance gap length was made larger to enhance resonance and the optical pad had dimensions of 12μm x 20μm. Due to the bimorph arms the room temperature angle of the cantilever with respect to the substrate was 50 degrees for the 95GHz pixel and about 5 degrees for the 693GHz pixel.

Fabrication

The THz detectors were fabricated using surface micromachining technology in a four step process. First, a 200 nm SiNx layer is deposited on a silicon substrate. The 10 nm/50 nm Ti/Au layer defining the SRR absorbers, readout reflector, and cantilever legs is then fabricated using standard lithography and liftoff processes. Next, the SiNx layer is patterned using lithography and plasma etching to define the MM supporting membrane

as well as the cantilever legs. Finally, the structures are released through backside KOH etching of the underlying silicon substrate. Fig. 2.2.2 shows an SEM image of a fully fabricated and released 95 GHz pixel. Figures 2.2.3 and 2.2.4 show dimensions and SEM image of pixels designs for 693 GHz operation.

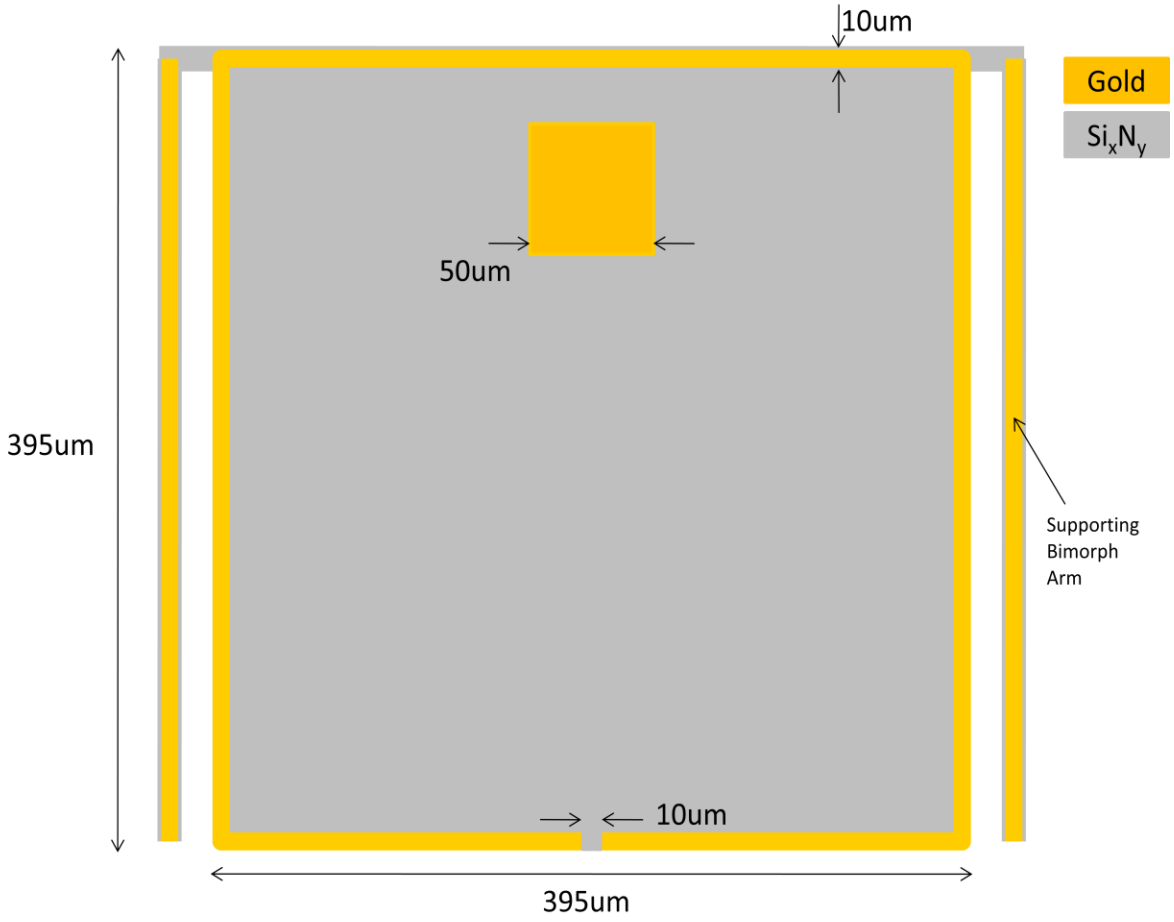

Fig. 2.2.1: Schematic layout and dimensions of 95GHz Pixel

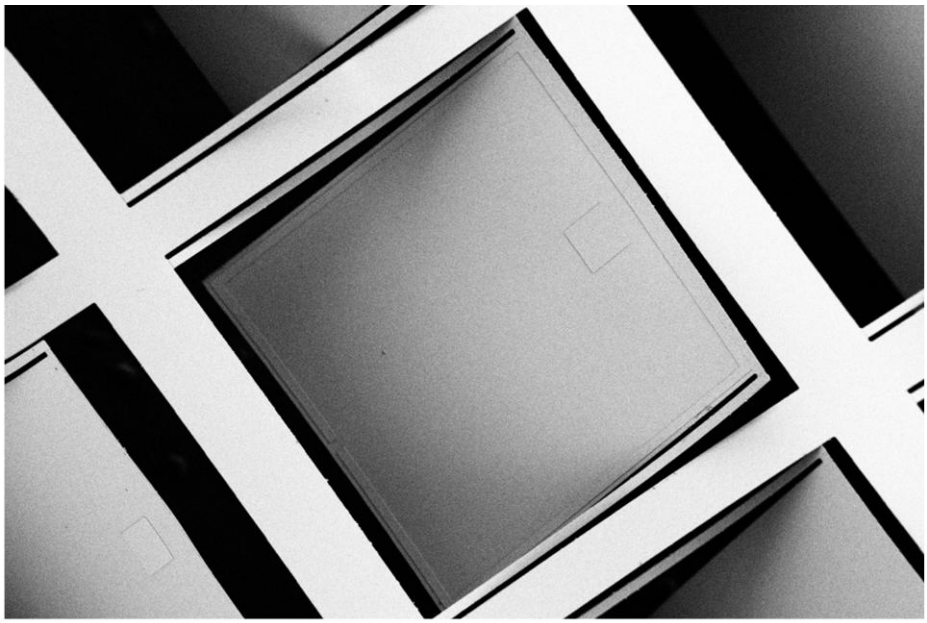

Fig. 2.2.2: SEM image of 95GHz Pixel

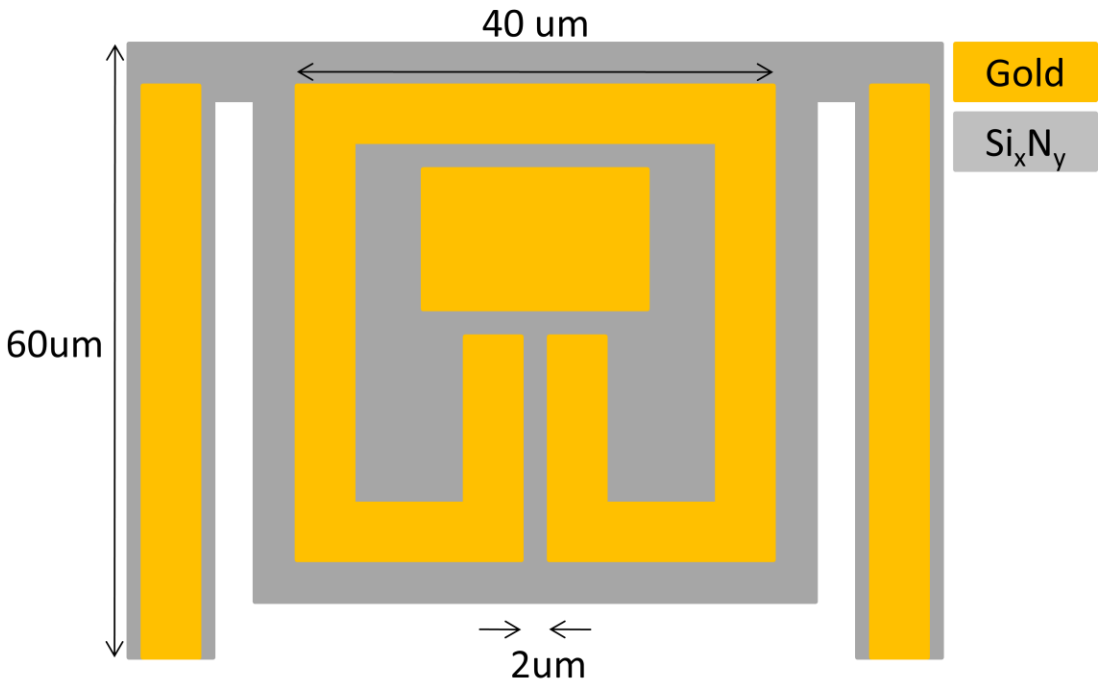

Fig 2.2.3: Dimensions of 693GHz pixel

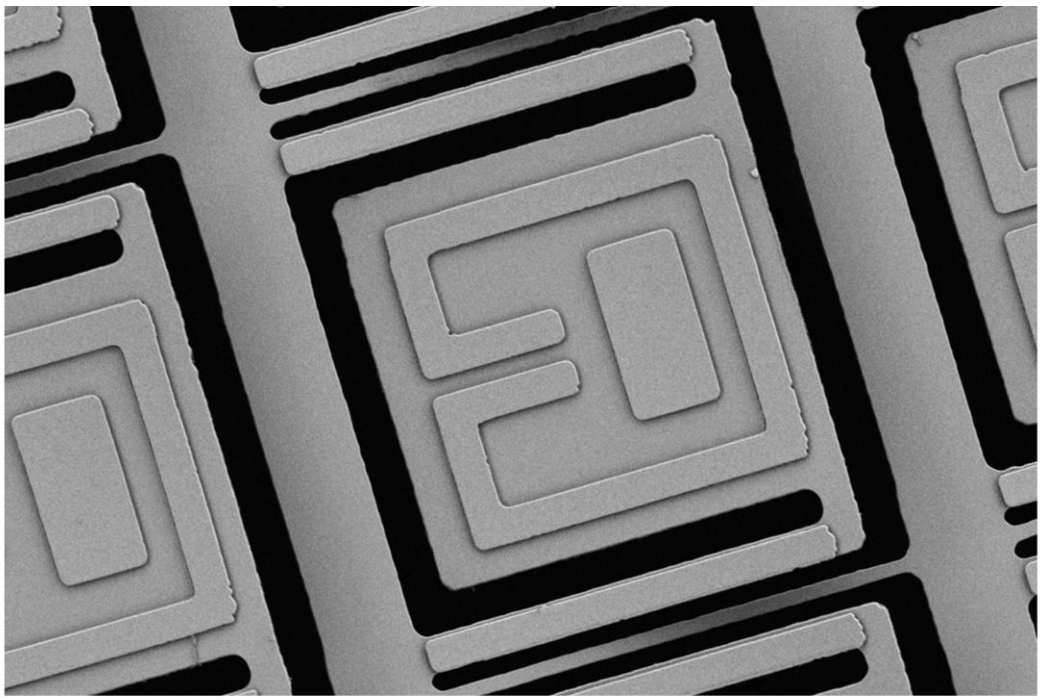

Fig. 2.2.4: SEM image of 693GHz pixel

THz-TDS measurement

THz Time-Domain spectroscopy (THz-TDS) measurements are a well-known and widely used method for measuring THz responses of materials. To measure the transmission response of the 95 GHz and 693 GHz samples a Picometrix TDS system was used. **Error! Reference source not found.** shows the measured transmission of the 95 GHz SRR samples. Being that TDS is well known and supported it is a good baseline to evaluate the characteristic response of the SRR pixels.

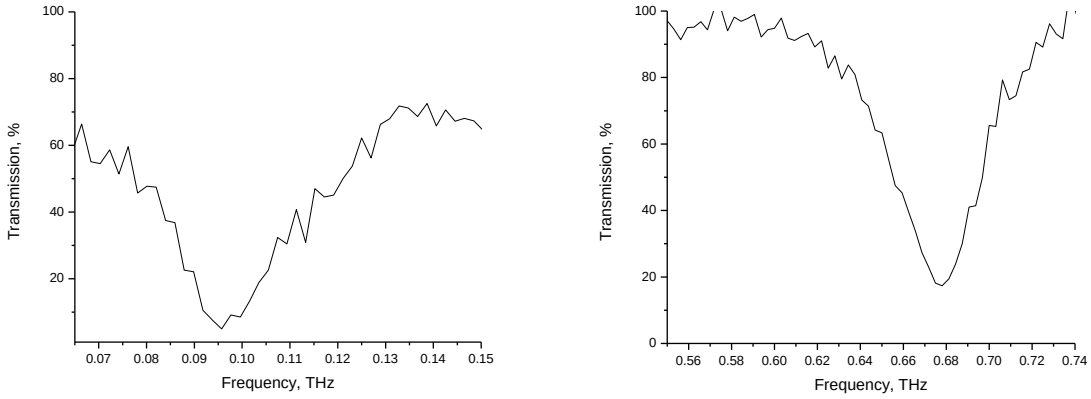

Fig. 2.2.5: TDS Transmission Measurement of 95 GHz and 693 GHz samples

An optical measurement apparatus was built for the measurement of the 95 GHz and 693 GHz samples. This device was made using Thorlabs cage mount parts consisting of a beam collimator, 5x beam expander, beam splitter, a 20x microscope objective for focusing, and a position sensitive detector (PSD) to measure the movement of the reflected beam. This device is easily mounted on a lab jack for mobility and height adjustment. The PSD electronics were purchased from Hamamatsu.

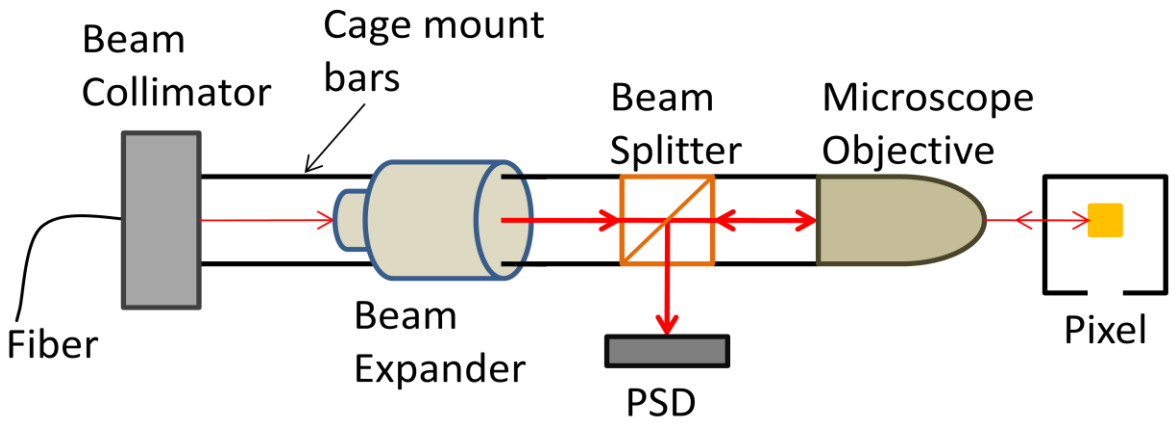

Fig. 2.2.6: Layout of Optical measurement apparatus

THz Source

The THz source used for the illumination of the 95 GHz pixels was manufactured by Virginia Diodes Incorporated (VDI). The source consisted of an Yttrium iron garnet (YIG) oscillator with a frequency range of 20 – 40 GHz controlled by a user-supplied voltage of 0 – 10 Volts. The output of the YIG oscillator is connected to a 10 dB coupler for frequency readout. The other output connection of the coupler is connected to an amplifier which is connected to a 3x frequency multiplier. The 3x frequency multiplier is connected to another amplifier to increase the output power. This is the basic configuration which supplies a frequency range of 75 – 110 GHz. Other frequency bands may be obtained by the connection of other sets of frequency multipliers. Other possible bands include: 140 – 230 GHz, 210 – 345 GHz, 280 – 460 GHz, 420 – 690 GHz, and 700 – 1000 GHz. The VDI source also contains the ability for user attenuation and the input off a TTL signal for square-wave chopping of the source.

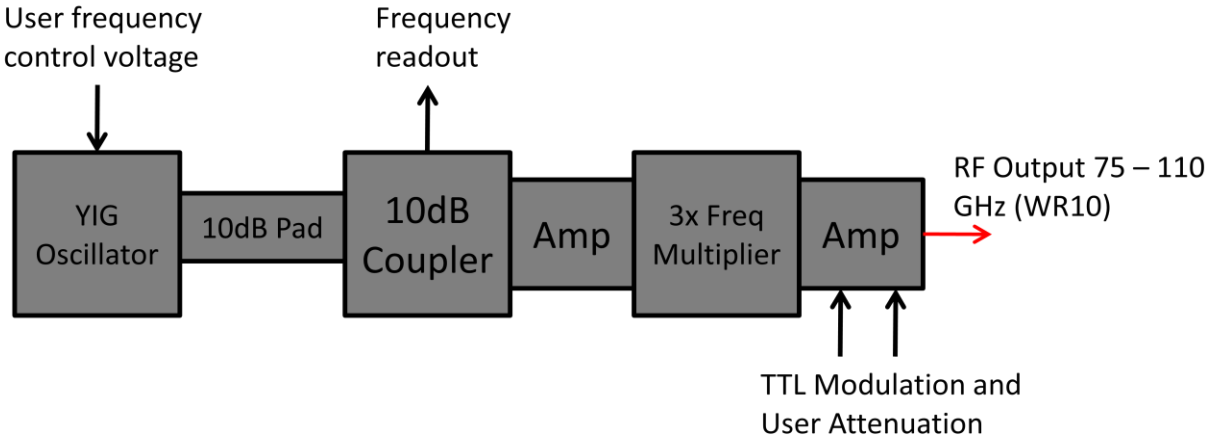

Fig. 2.2.7: Basic setup of VDI THz tunable THz source

To correctly measure the response of the 95 GHz sample the power spectrum of the THz source must be known. A Thomas Keating power meter was used for these measurements. **Error! Reference source not found.**.2.8 shows the power spectrum of the VDI THz source. It turns out that, even though the VDI source was adequate for these particular measurements, it had a faulty amplifier which caused the power to cut out at certain frequencies. This impacted the measurements in that extra care was needed in normalizing data to the incident power.

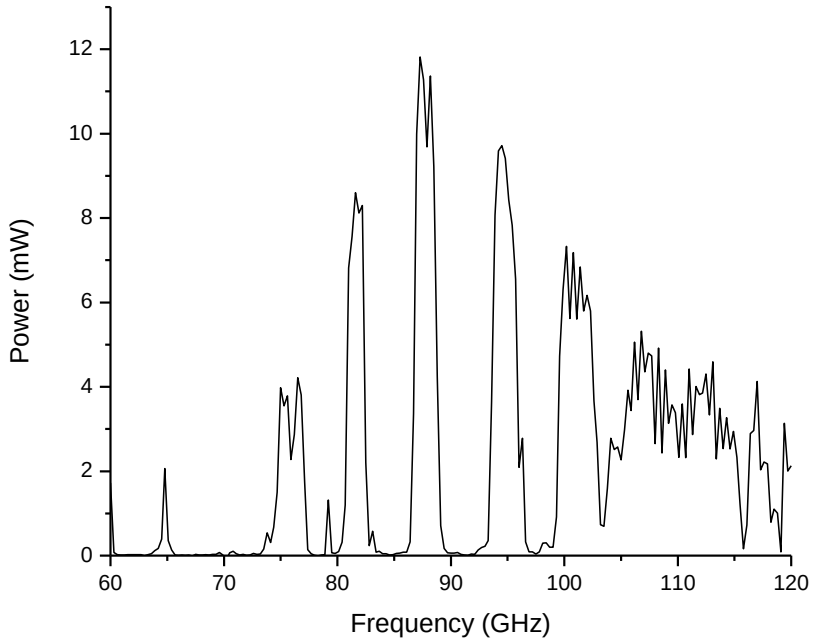

Fig. 2.2.8: Power Spectrum of VDI THz Source. The nulls in the emission were due to a faulty amplifier unit.

95 GHz response

A 12 inch diameter, 18 inch focal length lens was used to focus the microwave beam onto the SRR sample. The beam spot produced was 1.1 cm as measured using a the Pyrocam III beam imager. This provided ample room for equipment needed to support the sample. To hold the sample and provide a means for stabilization of the cantilever a sample box was made with the use of two high THz transmission windows and a Thorlabs cage mount box. This sample holder also provided a way to supply vacuum to the sample therefore creating higher thermal resistance of the cantilever system. Figure 2.2.9 shows the sample holder under measurement conditions. Due to built in stresses in the cantilevers, the experiment needed to be performed at approximately 50 degrees.

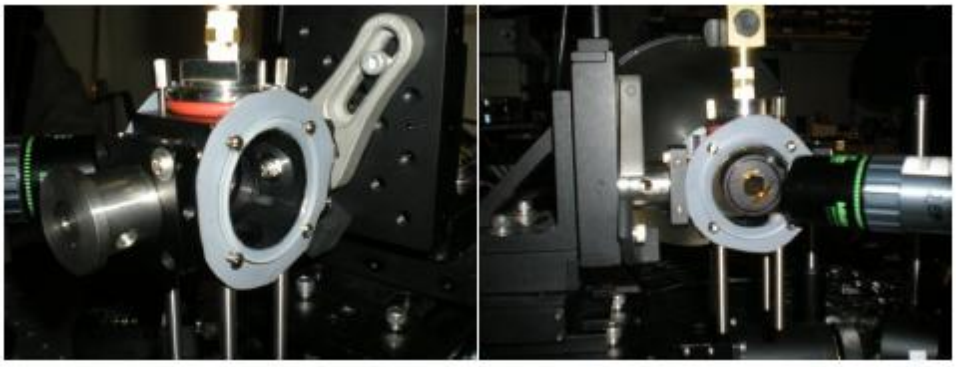

Fig. 2.2.9: Sample holder for bimorph cantilever samples.

To ensure that the measurement beam was reflecting off of the optical pad of the 95 GHz SRR a fiber light source was used to illuminate the back of the sample to view the sample through the measurement apparatus. For viewing of the sample the PSD was replaced with a CCD camera. This view provides a look at where the measurement beam resides on the SRR and also if the measurement apparatus is aligned perpendicular to the SRR. Once the reflector pad is found the CCD camera is then replaced with the PSD.

Measurement results

To ensure that the measurement beam was reflecting off of the optical pad of the 95 GHz detector a fiber light source was used to illuminate the back of the sample for viewing with the optical measurement apparatus. For viewing of the sample the PSD was replaced with a CCD camera. This image provided a view of where the measurement beam resides on the SRR and also if the optical measurement apparatus is aligned perpendicular to the SRR. Once the reflector pad is found the CCD camera is then replaced with the PSD. The THz source was square-wave modulated using a TTL signal. A lock-in amplifier was used to recover the signal of the detector. Due to the thermal characteristics of the device, a chopping frequency between 5 and 30 Hz was used to insure maximum heating response. The resonant nature of the detector was measured by scanning the frequency of the THz source and recording the optical signal of the detector. As shown in fig. 2.2.10, both polarizations were measured and only the polarization having the electric field arranged to drive the capacitor gap yielded a significant response.

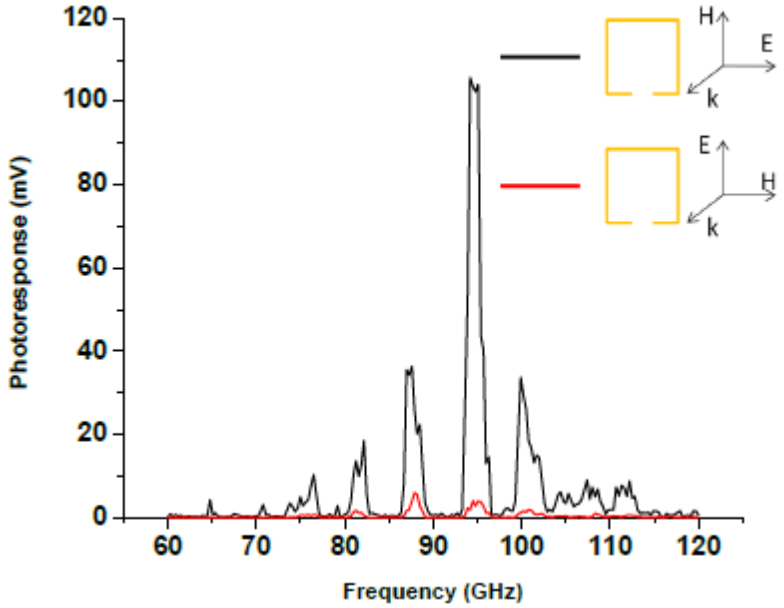

Fig. 2.2.10: Optical Response of 95 GHz Pixel to polarized incident radiation

The complete characterization of the 95 GHz detector platform is summarized in Fig. 2.2.11. Here, the photoresponse is referenced to the per pixel incident power using only the datapoints where the VDI source was operating at its full power. The resulting data points were then fit with a Lorentzian curve.

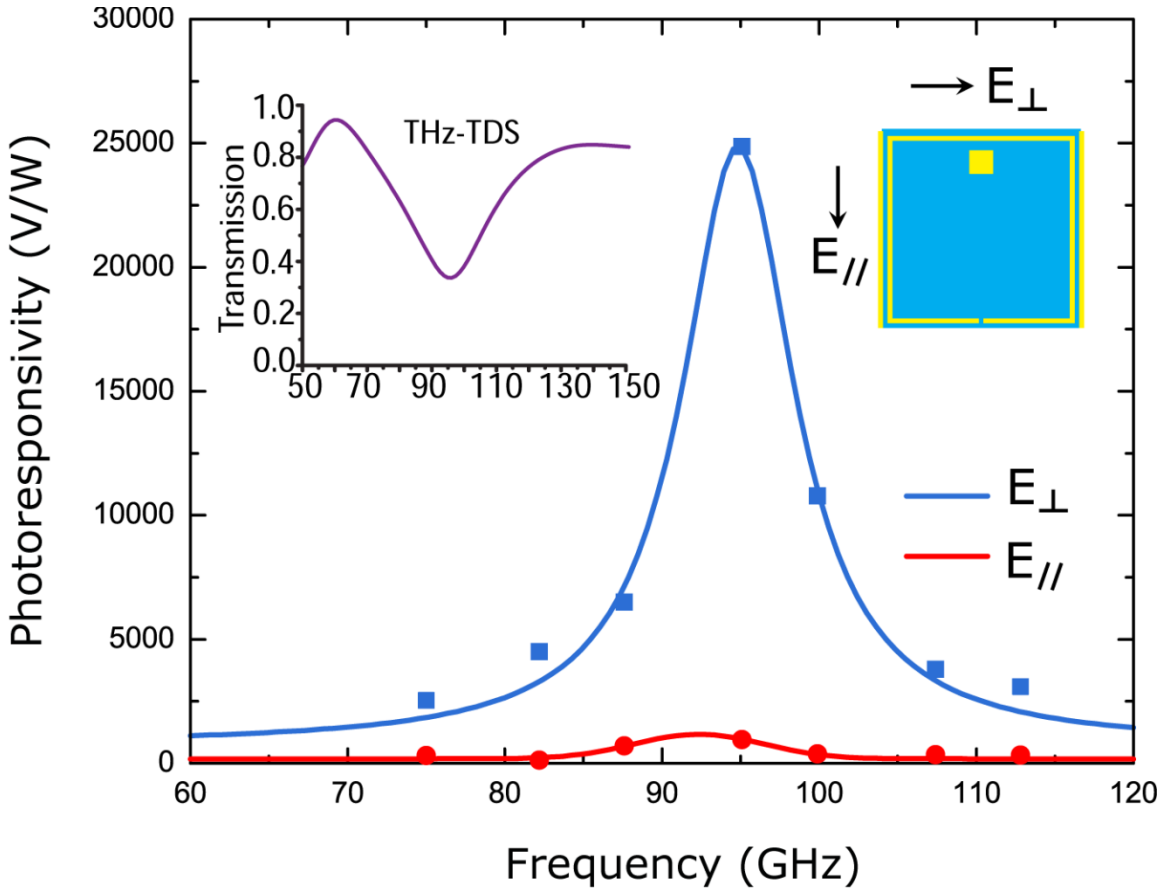

Fig. 2.2.11: Complete characterization of 95 GHz detector. Top left inset is THz-TDS spectra of array. The spectral data is referenced to measured incident power on a single pixel and reported here as responsivity.

693 GHz Sample

The same optical measurement device and sample holder was used as with the 95 GHz sample. The 693 GHz pixel when released has a small built in deflection angle between of only a few degrees, which greatly simplified device interrogation. Due to this small angle a different technique is used to locate an optical pad. Using Thorlabs motorized stages a xyz-motor controlled stage was built and programmed using LabView to locate the pad of a 693 GHz pixel. By measuring the transmitted measurement beam through the sample and scanning in the x-z plane the pads were easily located. **Error! Reference source not found.** shows a resultant scan of the LabView program to locate the 693 GHz pixel optical pad.

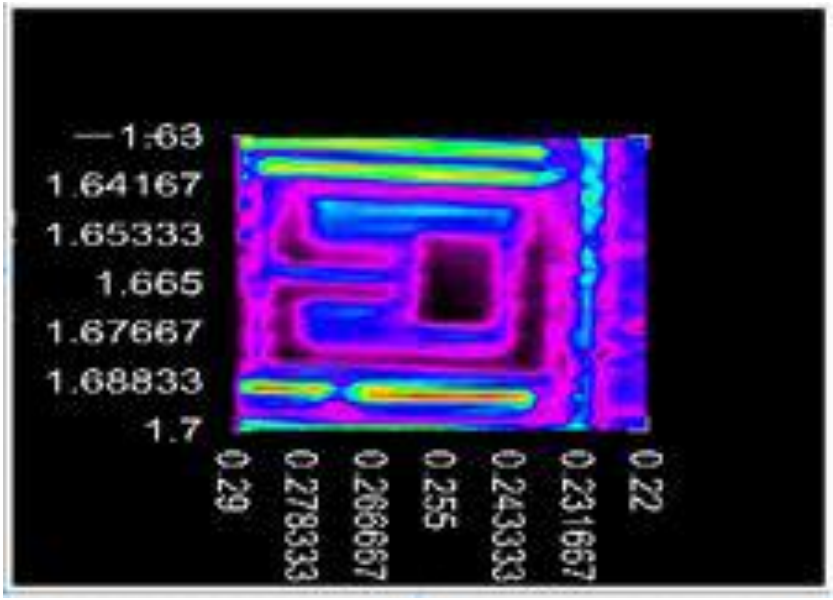

Fig. 2.2.12: Resultant Image of Pad Location Scan, the Pad is seen in the middle of the image.

Although the VDI source can be used to obtain a frequency of 693 GHz it was not used because of the low power in that frequency range. Instead a far infrared laser (FIRL) using a formic acid line pumped with a CO_2 laser was used as the illumination source. Although the frequency cannot be scanned the FIRL provides very good power, the maximum achieved was about 10 mW. A parabolic mirror was used to focus the beam onto the sample. To show good SRR characteristics the pixel must have a linear response and must be polarization dependent for this particular design. Two wire-grid polarizing optics were placed together to control the output polarization and power. The output of the FIRL is polarized in the vertical direction so to provide power control a second polarizer was placed in the vertical polarization. The first polarizer may be swept from vertical to horizontal for power attenuation. Combined with a second polarizer for polarization control, the power transmitted goes as $\cos^4(\theta)$, where θ is the angle of the first polarizer referenced to the horizontal plane. **Error! Reference source not found.** (a) shows the plot of optical response vs. incident power on the sample. The noise floor of the system was 0.43 mV. As shown in the plot that the SRR detector has a linear response with respect to power.

While the readout approach utilized could be significantly improved, we performed beam profiling measurements with the 693 GHz pixels in order to demonstrate the utility of our detectors, even at this stage, for THz beam diagnostics. In Fig.2.2.13 (b), we show beam measurements taken using a single pixel while the beam was steered along both axes. To capture the beam along the y-axis, the focusing paraboloid was simply translated. In a similar way, the x-axis data was captured by rotating the focusing optic. The result was a Gaussian profile similar to that measured with the commercial beam imager. While this is by no means an ideal technique for characterizing the beam, it demonstrates that these relatively simple detector elements can immediately find lab applications should an appropriate multi-pixel readout scheme be implemented.

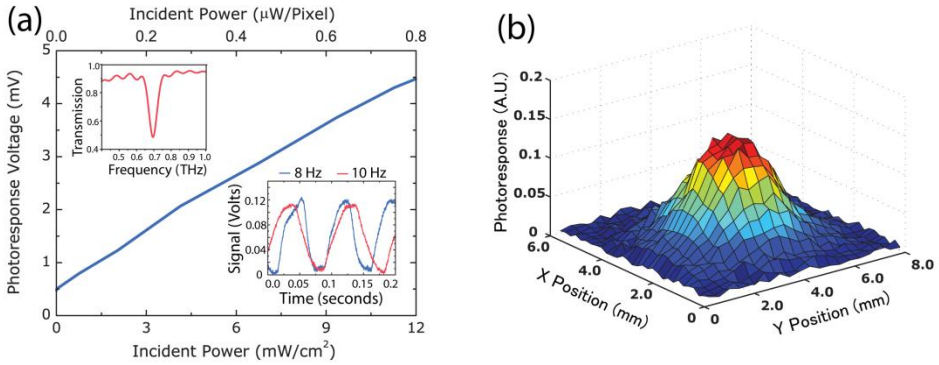

Fig. 2.2.13: Photoresponse of the 693 GHz detector. Top left inset in (a) is the THz-TDS characterization of the array while the bottom right inset is the temporal response to the modulated FIRL source. The main figure in (a) shows the linear response of the detector vs. incident power. (b) Beam image acquired by scanning the Gaussian FIRL beam over a single monitored pixel of the array.

3. CONCLUSIONS

The performance of the TMFPA platform was verified to be competitive with commercial microbolometer sensitivity while having a response time approximately 5 times faster. During this effort, multiple concepts were developed for improving sensitivity further although these will require extended dedicated effort. The metamaterial enhanced cantilever detectors demonstrated in this effort are naturally fabricated in array form and are suitable for real-time 2D imaging by simultaneously measuring the deflection of all of the pixels using, for example, a visible CCD/CMOS camera to obtain an intensity map for parallel pixel readout[20-21]. Furthermore, it is possible to combine multiple SRRs with different resonant frequencies into a super pixel, thus enabling frequency-sensitive THz imaging/spectroscopy with a "multicolor" THz illumination source. The optimal design of THz focal plane imaging detectors will also need to consider pixel size for particular imaging needs such as speed and sensitivity. For example, the MM unit cells are typically $\lambda/5 \sim \lambda/10$ in size. One may desire to have multiple MM SRRs constructed on a sensing pixel element that is matched to the optics of the overall system for optimum response[22]. While we demonstrated detection at 95 GHz and 693 GHz, in principle this approach can be applied to other unconventional wavelengths (even mid-IR) where nature does not provide us with appropriate material resonances amenable to integration with thermal detection platforms. There is also no reason that this basic concept using artificial absorbers could not be extended to TMFPA or conventional microbolometers. The implementation of low cost thin film THz absorbers could enable rapid progress in extending the many benefits of uncooled thermal imaging devices to the THz portion of the spectrum.

4. REFERENCES

1. Densmore, A., et al., *Sensitive label-free biomolecular detection using thin silicon waveguides.* Advances in Optical Technologies, 2008: p. 725967 (9 pp.).
2. Xu, D., et al., *Silicon photonic wire devices for biosensing and communications.* 2010 Asia Communications and Photonics Conference and Exhibition (ACP 2010), 2010: p. 52.
3. Watts, M.R., M.J. Shaw, and G.N. Nielson, *Optical resonators - Microphotonic thermal imaging.* Nature Photonics, 2007. **1**(11): p. 632-634.
4. Suzuki, K., K. Takiguchi, and K. Hotate, *Monolithically integrated resonator microoptic gyro on silica planar lightwave circuit.* Journal of Lightwave Technology, 2000. **18**(1): p. 66-72.
5. Wright, J., *High Quality Factor Silicon Nitride Ring Resonators for Biological Sensing*, in *Electrical Engineering*. 2010, University of New Mexico: Albuquerque

6 P. L. Richards, "BOLOMETERS FOR INFRARED AND MILLIMETER WAVES," Journal of Applied Physics, vol. 76, pp. 1-24, Jul 1994.

7 M. R. Watts*, et al.*, "Microphotonic Thermal Detectors and Imagers," in *Laser Resonators and Beam Control Xi*. vol. 7194, A. V. Kudryashov*, et al.*, Eds., ed Bellingham: Spie-Int Soc Optical Engineering, 2009.

8 W. Radford*, et al.*, "Sensitivity improvements in uncooled microbolometer FPAs," in *Infrared Technology and Applications Xxv*. vol. 3698, B. F. Andresen and M. S. Scholl, Eds., ed Bellingham: Spie-Int Soc Optical Engineering, 1999, pp. 119-130.

9 D. R. Smith*, et al.*, "Composite medium with simultaneously negative permeability and permittivity," *Physical Review Letters,* vol. 84, pp. 4184-4187, 2000.

10 V. G. Veselago, "ELECTRODYNAMICS OF SUBSTANCES WITH SIMULTANEOUSLY NEGATIVE VALUES OF SIGMA AND MU," *Soviet Physics Uspekhi-Ussr,* vol. 10, pp. 509-&, 1968.

11 D. Schurig*, et al.*, "Metamaterial electromagnetic cloak at microwave frequencies," *Science,* vol. 314, pp. 977-980, 2006.

12 B. I. Wu*, et al.*, "A study of using metamaterials as antenna substrate to enhance gain," *Progress in Electromagnetics Research-Pier,* vol. 51, pp. 295-328, 2005.

13 C. M. Bingham*, et al.*, "Planar wallpaper group metamaterials for novel terahertz applications," *Optics Express,* vol. 16, pp. 18565-18575, 2008.

14 T. J. Yen*, et al.*, "Terahertz magnetic response from artificial materials," *Science,* vol. 303, pp. 1494-1496, 2004.

15 A. N. Grigorenko*, et al.*, "Nanofabricated media with negative permeability at visible frequencies," *Nature,* vol. 438, pp. 335-338, 2005. 10.

16 D. R. Smith, W. J. Padilla, D. C. Vier, S. C. Nemat-Nasser, and S. Schultz, "Composite Medium with Simultaneously Negative Permeability and Permittivity," Phys. Rev. Lett. 84, 4184 (2000).

17 N. I. Landy, S. Sajuyigbe, J. J. Mock, D. R. Smith, and W. J. Padilla, "Perfect Metamaterial Absorber," Phys. Rev. Lett. 100, 207402 (2008).

18 H. Tao, N. I. Landy, C. M. Bingham, X. Zhang, R. D. Averitt, and W. J. Padilla, "A Metamaterial Absorber for the Terahertz Regime: Design, Fabrication and Characterizationm," Optics Express 16, 7181 (2008).

19 J. Hao, J. Wang, X. Liu, W. J. Padilla, L. Zhou, and M. Qiu, “High Performance Optical Absorber Based on a Plasmonic Metamaterial,” Appl. Phys. Lett. 96, 251104 (2010).

20 Q. Zhang, Z. Miao, Z. Guo, F. Dong, Z. Xiong, X. Wu, D. Chen, C. Li, and B. Jiao, "Optical Readout Uncooled Infrared Imaging Detector Using Knife-edge Filter Operation," Optoelectronics Letters 3, 119 (2007).

21 Y. Zhao, M. Mao, R. Horowitz, A. Majumdar, J. Varesi, P. Norton, and J. Kitching, "Optomechanical Uncooled Infrared Imaging System: Design, Microfabrication, and Performance," Journal of Microelectromechanical Systems 11, 136 (2002).

22 X. Liu, T. Starr, A. F. Starr, and W. J. Padilla, “Infrared Spatial and Frequency Selective Metamaterial with Near-Unity Absorbance,” Phys. Rev. Lett. 104, 207403 (2010).

Distribution

1	MS0359	D. Chavez, LDRD Office	1911
1	MS0782	K.L. Linker	6630
1	MS1080	M. Shaw	1719
1	MS1084	D.C. Trotter	1748
1	MS1415	E.A. Shaner	1123
1	MS1421	J.A. Simmons	1120
1	MS1423	G.A. Hebner	1128
1	MS1427	J.C. Barbour	1100
1	MS0899	Technical Library	9536 (electronic copy)


Sandia National Laboratories